

DOI: 10.1002/ ((please add manuscript number))

Article type: Full Paper

Hot-spot Engineering in 3D Multi-branched Nanostructures: Ultrasensitive Substrates for Surface Enhanced Raman Spectroscopy

Manohar Chirumamilla, Anisha Chirumamilla, Alexander S. Roberts, Remo Proietti Zaccaria, Francesco De Angelis, Peter Kjær Kristensen, Roman Krahne, Sergey I. Bozhevolnyi, Kjeld Pedersen, and Andrea Toma**

Dr. M. Chirumamilla, Dr. P. Kjær Kristensen, Prof. K. Pedersen

Department of Physics and Nanotechnology, University of Aalborg, Skjernvej 4A, Aalborg, 9220, Denmark

E-mail: mch@nano.aau.dk

Dr. A. Chirumamilla, Prof. R. Proietti Zaccaria, Dr. F. De Angelis, Dr. R. Krahne, Dr. A. Toma,

Istituto Italiano di Tecnologia, Via Morego 30, Genova, 16163, Italy

E-mail: andrea.toma@iit.it

Mr. A. S. Roberts, Prof. S. I. Bozhevolnyi

Institute of Technology & Innovation, University of Southern Denmark, Niels Bohrs Allé 1, Odense, 5230, Denmark

Keywords: Hotspot engineering, 3D multibranch nanostar structures, plasmonics, electron beam lithography, Single Molecule Surface enhanced Raman scattering

Abstract

The detection of probe molecules at ultralow concentrations, even at the single-molecule level, can be addressed with the breakthrough concept of plasmonic hot-spot engineering. In view of that, the fabrication of nanostructures endowed with sub-10 nm gaps and extremely large near-field enhancement has gained increasing attention, becoming a key-condition for improved sensitivity. The present work demonstrates a new perspective in ultrasensitive detection by engineering every individual plasmonic nanostructure with a giant electric field confinement and superior hot-spot densities, thus eliminating the need for extremely narrow inter-particle separations.

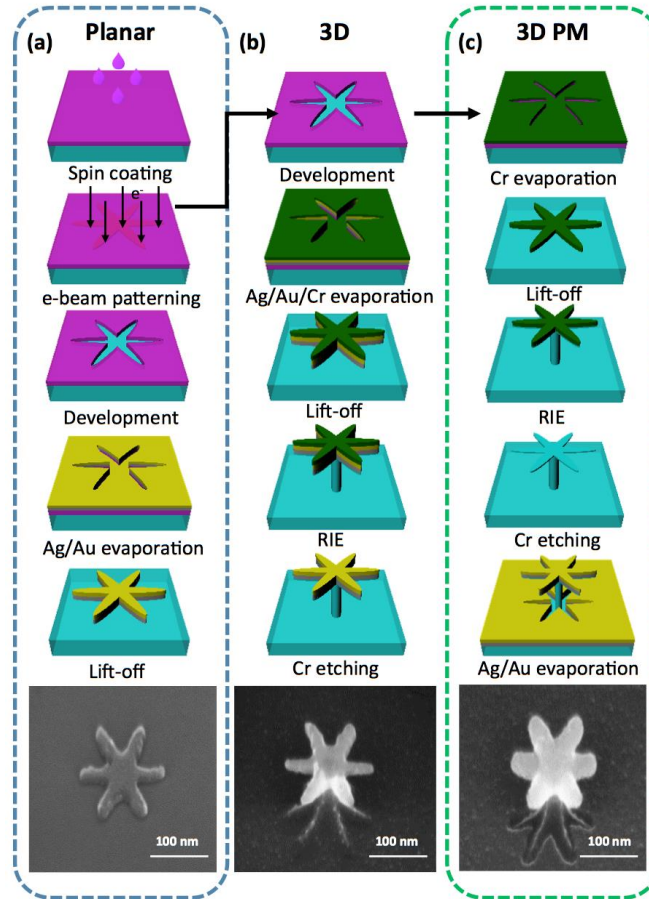
1. Introduction

The manipulation of strongly enhanced and localized electromagnetic (EM) fields, i.e. hot-spot engineering, is a consolidated concept in plasmon-based molecular

sensing.^[1] Among them, surface enhanced Raman spectroscopy (SERS) provides label-free detection of analytes down to the single-molecule level by making use of hot-spots with high sensitivity and specificity.^[2-5] In SERS, the weak Raman signals are enhanced by many orders of magnitude (up to 10^7 or higher) due to the interaction between molecules and optical near-fields confined to and enhanced by plasmonic nanostructures. In view of that, positioning probe molecules in the vicinity of hot-spots is crucial for improving the SERS enhancement factor and therefore the detection limit.^[2, 6, 7] For instance, Le Ru et al.^[8] have shown that, for a system of silver particle dimers, 98% of the SERS signal is provided by only 2% of the molecules adsorbed at positions with strongly enhanced EM fields. It is therefore imperative for sensing applications at ultralow molecule concentrations to design and fabricate nanostructures featuring sufficiently high hot-spot densities. So far, nanostructures arranged in the form of dimers, arrays or clusters with separations of few nanometres have been used to engineer single/multiple hot-spots.^[9, 10] However, the fabrication methods employed, whether bottom-up or top-down, suffer from irreproducibility and non-uniformity, due to practical limitations such as gap diffusion, proximity effect, agglomeration, etc.^[11] These difficulties call for alternative platforms in order to develop ultrasensitive SERS substrates, among which single plasmonic nanostructures with multiple branches and sharp protrusions are ideal candidates. In fact, the present architectures can sustain large hot-spot densities with precisely defined spatial locations, thus eliminating the need for sub-10 nm gaps in single/few molecules detection.^[12]

Multi-branched nanostructures can be realized by various methods, including colloidal and top-down approaches.^[7, 13] Colloidal techniques provide metal nanoparticles with sharp tips but are still of limited capabilities with respect to the number of branches, spatial control of their placement, and uniformity, all of which hamper reproducible SERS applications. The poor spatial control over the formation of

hot-spots can significantly be improved by fabricating multi- branched nanostructures with lithographic methods and thereby realizing uniformly patterned (in terms of morphology and interparticle separation-IPS) periodic nanostructures.^[14]



Scheme 1. a-c) Schematic representation of the fabrication protocol for 6 branch nanostructures with planar, 3D and 3D PM topologies. The corresponding fabricated nanostructures are shown in the SEM images.

Furthermore, the substrate supporting the nanostructures plays a key factor in determining the hot-spot strength.^[15, 16] The vast majority of plasmonic nanostructures are fabricated on conventional bulk dielectric substrates. This causes strong EM field interactions between the nanostructure and the underlying material, thus reducing the near-field enhancement. In recent works, it has been demonstrated that nanostructures residing on nano-pedestals (three-dimensional nanostructures) can enhance the strength of optical near-fields by orders of magnitude as compared to the corresponding planar (two-dimensional) counterparts (**Scheme 1a**).^[3, 17, 18] Therefore, in the present work,

3D multi-branched nanostructures (3D MBNS) with number of arms from 4 to 10 (in the following named S4 to S10) detached from dielectric substrates, and/or perforated metal (PM) layers were systematically engineered for achieving the best combination of hot-spot density and optical near-field enhancement. The corresponding topologies have been schematically illustrated in Scheme 1b and c. To this end, planar and 3D bimetallic (Au/Ag) plasmonic nanostructures with multiple-branches were fabricated by electron-beam lithography (EBL) and reactive ion etching (RIE) techniques. The advantage of double-layer Au/Ag nanostructures is the combination of high chemical stability and high field enhancement that cannot be provided by the single metal components.^[4, 19] The far-field and near-field optical responses of the nanostructures were experimentally evaluated by reflection and Raman spectroscopy. In particular, the formation of multiple hot-spots with strongly enhanced local EM fields and the subsequent detection of analyte molecules at ultralow concentrations (p-Aminothiophenol (p-MA) and Rhodamine-6G (R6G) down to 1 fM) have been demonstrated through SERS measurements.

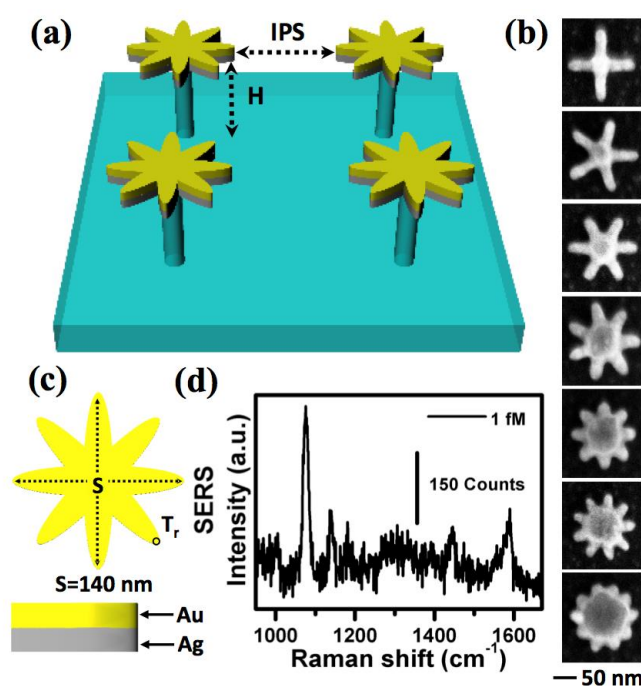


Figure 1. a, c) Schematic of bimetallic 3D MBNS structures for S8 layout, illustrating the geometrical parameters: silicon pillar height H , inter-particle separation IPS, tip radius T_r and structure size S . b) Representative SEM images (top view) of 3D MBNS with 4 to 10 branches (S4-S10 from top to bottom); every micrograph shares the same scale bar. d) SERS spectrum recorded from p-MA (chemisorbed from 1 fM concentrated solution) on 3D MBNS structure with S8 geometry.

2. Results and Discussion

The detailed protocol for the fabrication of planar, 3D and 3D PM structures with multi-branched geometry is presented in Scheme 1a-c and described in the experimental section. The corresponding SEM images (54° tilted view) of the fabricated nanostructures have been placed at the bottom of each panel, highlighting the difference between the various topologies. For 3D PM nanostructures, metallic perforations are clearly visible in the SEM image (Scheme 1c). To avoid strong near-field coupling between the individual unit of the array, a 200 nm IPS was chosen. In order to explore the effect of topology on the plasmon resonances, the height (H), size (S) and tip radius (T_r) for all nanostructures have been fixed to 150, 140 and 10 nm, respectively (see the schematic illustration reported in **Figure 1a** and c). A typical SEM image of 3D MBNS structures for S8 geometry with 200 nm IPS and 340 nm array periodicity is displayed in Figure SI1, demonstrating their structural uniformity and spatial homogeneity. The morphology of nanostars with 4 to 10 branches is depicted in Figure 1b. The corresponding surface area has been extracted from the SEM images, obtaining a value of 4400 nm², 5500 nm², 6400 nm², 7300 nm², 9500 nm², 10100 nm² and 10700 nm², for the structures S4, S5, S6, S7, S8, S9 and S10, respectively. We notice that more than 10 branches are not feasible for 140 nm sized structures, since the individual protrusions are no longer well defined. Figure 1d illustrates a typical SERS spectrum of p-MA at 1 fM concentration deposited by chemisorption (see Experimental section) on the 3D MBNS with S8 geometry. The characteristic Raman modes at 1077 and 1590 cm⁻¹ are clearly visible and highlight the viability of the device for ultrasensitive Raman applications. Here the incident

laser wavelength, accumulation time, and power were set to 785 nm, 3 s and 1 mW, respectively, while the incident light polarization was fixed parallel to the x-direction.

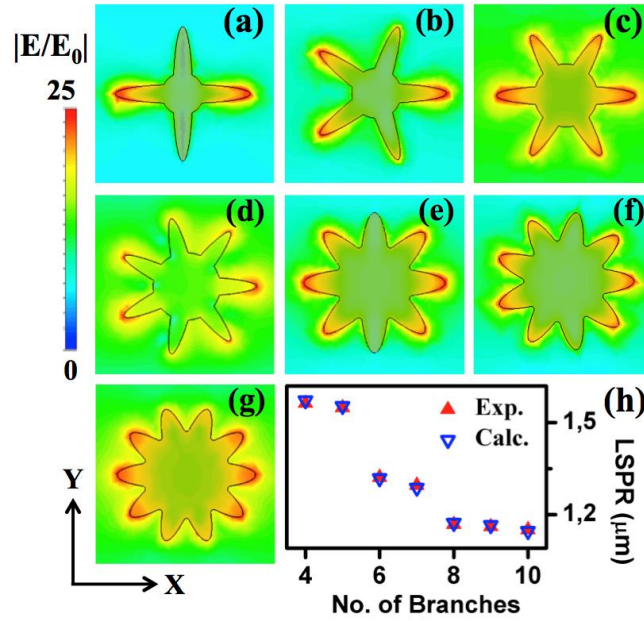


Figure 2. a-g) The total electric field distribution of planar MBNS for S4-S10 architectures obtained at a distance of 1 nm above the nanostructure for their characteristics LSPRs (h) in the x-y plane. The illuminating EM field is polarized along the x-direction.

In order to assess the number of branches effect on the hot-spot formation and plasmonic behaviour, the near-field distribution (Computer Simulation Technology-Microwave, CST-MW) and far-field response (Synopsys' Optical Solutions, RSoftTM) of MBNS were numerically simulated. In particular, the near-field behaviour has been evaluated through finite integration technique (FIT) while far-field response was determined through rigorous coupled wave analysis (RCWA). Indeed, while the former approach is very suitable for determining the electromagnetic field distribution within sub-wavelength structures, the latter one is particularly convenient for evaluating the transmission/reflection/absorption spectra of periodic structures. **Figure 2a-g** show the electric field enhancement ($|E/E_0|$) distribution of S4-S10 planar nanostructures in correspondence of their localized surface plasmon resonance (LSPR). The relative wavelengths have been reported in Figure 2h (blue triangles). Two hot-spots along the

incident polarization direction (x-axis) are clearly visible for the S4 configuration (Figure 2a). An increase in the hot-spot density is observed when raising the number of branches, accompanied by a strong blue-shift in the LSPR position (Figure 1h).^[20]

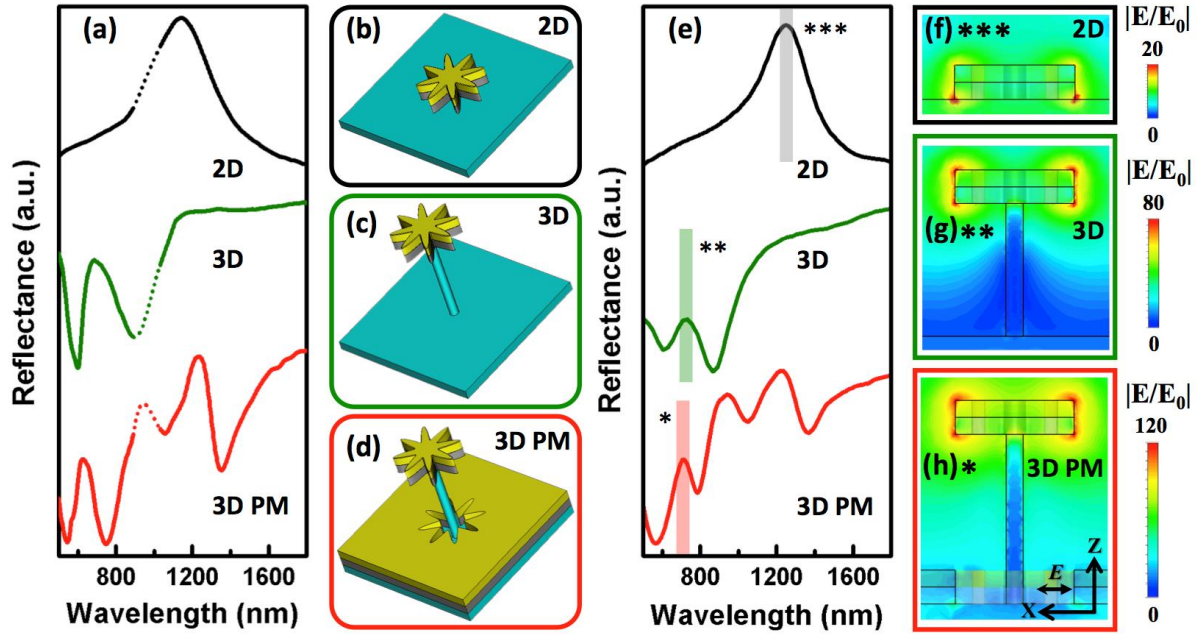


Figure 3. a) Experimental reflectance spectra for S8 architectures with planar, 3D and 3D PM topologies depicted by black, olive and red traces, respectively. The dotted lines are a guide to the eye bridging the spectral region not accessible by our experimental setup. b-d) Schematic representation of the different topologies. e) Simulated reflectance spectra of periodic S8 nanostructures with planar, 3D and 3D PM layouts. f-h) Electric near-field distribution in the x-z plane for S8 nanostructures shown in (a, e) at their characteristics LSPR position, 1165 nm (***) - grey band), 680 nm (**) - green band) and 650 nm (*) - red band) for planar, 3D and 3D PM layouts, respectively.

Reflectance measurements have been performed on MBNS (S4-S10) with planar and 3D architectures. **Figure 3a** shows the typical experimental results from planar and 3D architectures. **Figure 3a** shows the typical experimental results from planar, 3D and 3D with PM layer (for schematics, see Figure 3b-d) for S8 geometry. The reflectance spectra have been normalized with respect to the un-patterned area of the corresponding substrate. The experimental results match the theoretical calculations, reported in Figure 3e. For planar architectures (Figure 3a, black trace, resonating around 1165 nm), the local near-fields are confined at the interface between metal and bulk silicon substrate (Figure 3f), weakening the local EM field enhancement $|E/E_0| = 20$, and limiting the accessible regions (hot-spot volume) for

molecule detection. Surface plasmon resonances in high refractive index materials (such as silicon) are tightly confined within the substrate, resulting in low optical near-field strengths, low extinction-cross sections, large propagation losses and strong red-shifts with the broadening of resonances when compared to low refractive index materials (e.g. glass).^[15, 21] In order to avoid the confinement of the hot-spots into the bulk substrate and to create an effective low index medium, it is essential to engineer further the present layout. The contact area of the metallic nanostructure interacting with the dielectric substrate can be decreased by introducing a dielectric nanopedestal, which decouples the strong optical-near fields localized at the metal surface from the bulk substrate. Here RIE has been used to carve out the dielectric medium underneath the metallic nanostructures, thus promoting the formation of a thin, pedestal-like support structure (Figure 3c, d).

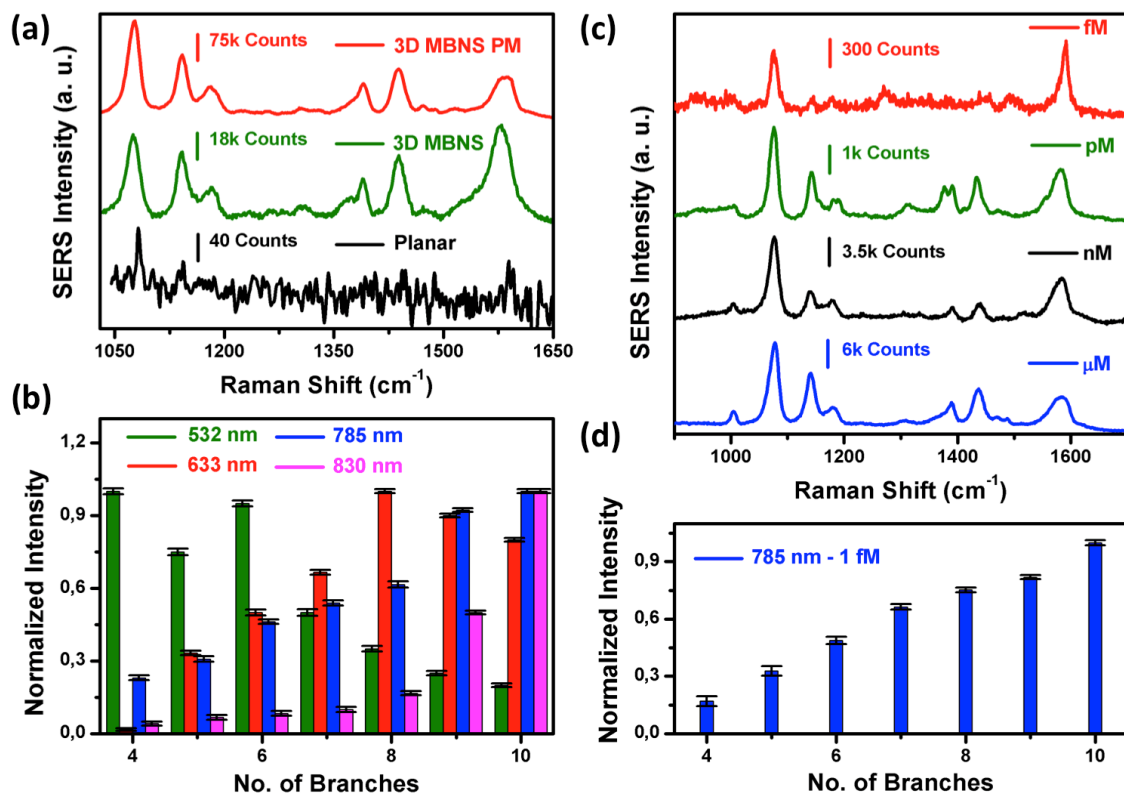


Figure 4. a) SERS spectra of p-MA chemisorbed at 1 μ M concentration obtained from S8 MBNS on planar, 3D and 3D PM topologies, black, green and red traces, respectively. b) SERS intensity variation of 1077 cm^{-1} band as a function of a number of branches for 532, 633, 785 and 830 nm laser excitation wavelengths. c) SERS

spectra recorded from p-MA molecules chemisorbed on 3D MBNS PM structures with S8 geometry at 1 μ M, 1 nM, 1 pM and 1 fM concentrations represented by red, blue, green and orange traces, respectively. d) SERS signal intensity versus a number of branches at 1 fM concentration for 785 nm laser excitation.

For 3D MBNS structures, a significant blue shift of LSPR (Figure 3a, e – green band in the olive trace) has been observed with a resonance maximum at around 680 nm. Numerical calculations show that the separation of the metal nanostructures from the bulk substrate leads to a significant EM field enhancement, $|E/E_0| = 80$ (Figure 2g). Furthermore, the nanopedestal introduction causes a huge blue-shift (around 485 nm) in the LSPR spectral position, since the plasmon resonance is very sensitive to the dielectric environment.^[17, 22, 23] The elevated 3D design has additional advantages in comparison with other works:^[22] the regions of enhanced EM fields are completely accessible to the probe molecules used in analytical techniques, and it offers a low effective dielectric medium along with the high chemical and structural stability of silicon. For 3D MBNS with PM layer structures, multiple resonances are observed in the reflection spectrum (Figure 3a, e-red trace). To elucidate the origin of these modes, near-field distributions were calculated and analyzed in Supplementary Information SI2 and SI3. It is worth noticing that the electric field (Figure 3h) and the surface current distributions (Figure SI2) at 650 nm show a dipolar behaviour with strong electric field localization at the nanostructure ends, thus confirming the LSP nature of this resonance. A slight variation in the nanostructure LSPR position (i.e. a blue-shift of 30 nm) with respect to the 3D configurations without PM layer is observed.^[24] To illustrate the PM role on the far-field response of the 3D MBNS PM nanostructure, numerical calculations were performed on the PM layer alone, without taking into account the complete 3D layout (Figure SI2c black trace, and SI3). The star-shaped hole in the PM layer behaves like a plasmonic cavity and allows the excitation of LSPR as well as surface plasmon polaritons (SPPs) propagating at the metal/air and

metal/substrate interfaces.^[25] A complete description of the modes supported by the structures is analyzed in Figure SI2 and SI3, where the near- and far-field responses have been investigated. Turning back to the 3D MBNS PM structures, we find that for the S8 architecture the resonances of the isolated PM layer and 3D structure can be clearly recognized (Figure 3a and e, red trace). SPP modes propagating at the two interfaces of the PM layer can be associated to the spectral features at 543 and 1050 nm, while the resonances at 620 and 1350 nm can be attributed to the LSPRs supported by MBNS and PM holes, respectively (a deeper investigation has been carried out in Figure SI3). Reflection spectra for morphological changes (from 4–10 branches) of 3D MBNS PM in the visible region are shown in Figure SI4.

The sensing performances of MBNS structures were evaluated by SERS measurements on the S8 geometry with p-MA molecules chemisorbed from 1 μ M solution concentration. Since the Raman enhancement scales with the 4th power of the field, 3D MBNS PM with an EM field enhancement factor of 120 can increase the Raman signals up to a factor of 10^8 .^[26] **Figure 4a** shows the SERS spectra from the S8 architectures with planar, 3D, and 3D PM layer topologies (black, olive and red traces, respectively). The laser excitation wavelength, power and accumulation time were set to 785 nm, 1 mW and 30 s, respectively, while the incident light was polarized along the x-axis. Strong and well-resolved characteristic Raman modes of p-MA centered at 1077, 1140, 1179, 1390, 1440 and 1590 cm^{-1} , corresponding to the molecular vibrations of C-S-stretching, C-H-bending, C-H-bending, C-H-bending+C-C-stretching, C-C-stretching+C-H-bending and C-C-stretching, respectively, are clearly visible for the 3D MBNS PM (red trace) structures.^[3, 4] For planar nanostructures, a low signal-to-noise ratio SERS spectrum (black trace) is observed. Two peaks centred at 1077 and 1590 cm^{-1} are identified in the spectrum with an intensity just above the noise level while the other bands are buried in the background noise. When the metal

1 nanostructures are elevated from the bulk substrate by a nanopedestal, the SERS signal
2 intensity increases significantly and the presence of characteristic Raman modes of p-
3 MA in the full spectral range is clearly observable in the olive trace. A further rise in
4 the SERS signal intensity has been obtained for 3D MBNS PM structures (red trace),
5 owing to the coupling of reflected light from the PM back-plane with the metallic
6 nanostructures. The observed SERS signal enhancement is in accordance with the rise
7 in the electric field enhancement, as confirmed by numerical calculations (Figure 3g
8 and h).

19 The 3D MBNS PM structures show an average enhancement of 5×10^6 , obtained by
20 evaluating the peak at 1077 cm^{-1} recorded from p-MA on substrates with S8 geometry (an un-
21 patterned area of the AgAu film has been used as a reference). The detailed method adopted
22 for the enhancement factor calculation has been reported in supplementary information. We
23 underpin that the planar AgAu film itself acts as SERS enhancing substrate and provides an
24 enhancement factor in the order of 10^4 (supporting information),^[27] hence the absolute
25 enhancement factor of the MBNS structures are estimated to be in the order of 10^{11} . The
26 uniformity of the substrate, reproducibility of the SERS signals and homogeneity of the
27 molecular deposition have been evaluated by taking SERS measurements (around 70 spectra)
28 on 3D MBNS PM structures with S8 geometry laid on the same substrate at different spatial
29 positions. A 3D waterfall SERS spectrum shows uniform signal intensity for each
30 characteristic band position (Figure SI5); the maximum standard deviation of SERS intensity
31 at 1077 cm^{-1} is less than 5%, which highlights the substrate reproducibility in terms of
32 uniform hot-spot density, and homogeneity of molecular chemisorption. To further
33 understand the influence of the hot-spots on the SERS intensity, Raman measurements were
34 performed on 3D MBNS PM structures (from S4 to S10) with four different excitation
35 sources. In order to get the same molecular surface absorption properties, nanostructures with
36 4-10 branches were fabricated on the same substrate. Figure 4b shows the SERS intensity of

the 1077 cm^{-1} band recorded with laser sources at 532, 633, 785 and 830 nm, depicted by green, red, blue and magenta bars, respectively. The SERS intensities have been independently normalized for each laser source with respect to the highest peak intensity obtained in the series. For 830 and 785 nm laser excitations, a monotonic increment in SERS signal intensity with increasing branch number can be observed, where the excitation source is out of resonance with the LSPRs (Figure SI4). In this case, the SERS signal intensity increases with the number of hot-spots. In the case of 633 nm excitation, the S8 architecture shows a significantly higher SERS signal intensity compared to other nanostructures, because the excitation wavelength approaches the LSPR of the S8 nanostructure. Similarly, the variations in the SERS signal intensity for 532 nm excitation can be understood in terms of closeness to the LSPR. SERS spectra of 3D MBNS PM structures with S8 geometry for different excitation sources demonstrate that such nanostructures enable fine-tuning of the SERS performance that can be adapted to a broadband of excitation wavelengths, which is of great advantage for practical SERS applications (Figure SI6).

Figure 4c presents the SERS spectra of p-MA molecules on the 3D MBNS PM structures with S8 geometry for concentrations ranging from 1 μM to 1 fM. The excitation wavelength, power and accumulation time are set to 785 nm, 1 mW and 3 s, respectively. The SERS spectra show clearly distinguishable characteristic peaks of p-MA with good signal to noise ratio. We note that for low concentrations only a limited number of molecules is available for adsorption on the metal nanostructures and therefore the SERS signal intensity decreases. The SERS spectrum from 1 fM concentration (orange trace) clearly shows two characteristic bands of p-MA at 1077 and 1590 cm^{-1} ; other modes are slightly above the noise level. Detection of p-MA molecules at 1fM concentration highlights the capabilities of the proposed substrate towards single/few molecule detection. Similarly, typical SERS spectra of R6G at different molecular coverage density are shown in Figure SI7. At 1 fM concentration,

the prominent peaks of R6G at 1364 and 1610 cm^{-1} are clearly distinguishable in the spectrum.^[4, 10] Figure 4d shows the SERS intensity (normalized with respect to 3D MBNS PM structures with S10 geometry for 1077 cm^{-1} band position) versus the number of branches for 785 nm laser excitation at 1 fM concentration. A monotonic rise in the SERS intensity is observed with an increasing in the number of branches from 4 to 10, due to a corresponding growth of the hot-spot density. Therefore, the number of branches and 3D topology play a key role in the SERS signal enhancement. The increased hot-spot density successfully boosts the SERS signal intensity at extremely low concentrations, and the detection of analyte molecules at 1 fM firmly establishes the ultrasensitive capability of the proposed 3D multi-branched nanostructures.

3. Conclusion

In summary, 3D multi-branched nanostars with perforated metal layers have been conceived and proposed as ideal platforms for high density hot-spot generation, particularly suitable for detection at extremely low concentration (1 fM), as demonstrated by SERS measurements on p-MA and R6G molecules. Our systematic study elucidates the influence of the number of branches on hot-spot generation, and the effect of dielectric substrate and underlying perforated metal layer on the far-field and near-field response. Tuning and optimization of the multi-branched nanostar structures with respect to the excitation sources enable average enhancement factors of 5×10^6 with good homogeneity over the entire device. These engineered SERS substrates pave the way towards the commercialization of ultrasensitive SERS devices through economically scalable manufacturing methods and cost-effective approaches.^[4] Moreover, the unique properties offered by multi-branched architectures, i.e. the realization of multiple hot-spots on a single nanostructure, envision clear-cut perspectives in hyperspectral Raman imaging, miniaturized Raman-on-chip

biomolecule detection and more in general for the development a new-era of sensing technology.

4. Experimental Section

Fabrication of multi-branched nanostructures: All presented MBNS structures are fabricated by electron-beam lithography (EBL–Raith 150-Two) and subsequent reactive-ion etching (RIE - SENTECH) techniques. A detailed protocol of the fabrication procedure along with SEM images is shown in the Scheme 1. Planar, 3D and 3D PM nanostructures have the EBL step in common. A 250 nm polymethyl methacrylate (PMMA) layer is formed by spin-coating an anisole based PMMA solution (PMMA-A2, average molecular weight 950 kDa, Micro Chem Corp.) at 3000 rpm for 60 s onto a p-type c-Si (100) wafer and subsequent baking (180 °C for 9 min on a hot plate). The PMMA is exposed (Raith 150-Two, operated with an acceleration voltage of 30 kV and a beam current of 130 pA) with an area dose of 1 mC/cm². The PMMA layer is then developed in a 1:3 mixture of methyl isobutyl ketone (MIBK) and isopropanol (IPA) ratio at 4 °C for 180 s.

To obtain planar nanostructures, a 36 nm thick bi-layer of 18 nm Au on 18 nm Ag is deposited. Excess resist and metal layers are removed by ultrasonically assisted lift-off in acetone. 3D nanostructures are fabricated by a first evaporating a bi-layer of Au-on-Ag (18 nm + 18 nm) and a subsequent thermal deposition of a 20 nm chromium layer. Ultrasonically assisted lift-off is then performed. Subsequently, the samples are reactive-ion etched in an atmosphere of SF₆ (30 SCCM) + C₄F₈ (32 SCCM) at 1 mTorr. The process parameters temperature, power, and etching time are held at 4 °C, 18 W and 25 s, respectively, which yields an etch rate of approximately 100 nm/min. The excess chromium film is then removed by a commercially available chromium etch (Sigma-Aldrich). 3D MBNS PM structures are obtained by depositing 20 nm of chromium after developing the EBL patterned substrates. After the deposition of chromium, acetone lift-off leaves behind star-shaped chromium patterns on silicon, serving as etching masks. RIE now shapes the pedestals supporting the

stars, and subsequently, the chromium mask is etched away, leaving behind silicon stars on poles. Finally, an Au-on-Ag (18/18 nm) bi-layer is evaporated at a deposition rate of 0.3 Å/s to form the resonators as well as the perforated film.

Numerical calculations: The near-field behavior has been evaluated through finite integration technique (FIT - Computer Simulation Technology-Microwave, CST-MW) while far-field response was determined through rigorous coupled wave analysis (RCWA - Synopsys' Optical Solutions, RSoft™). The former approach is very suitable for determining the electromagnetic field distribution within sub-wavelength structures; the latter one is more specific for providing the transmission/reflection/absorption spectra of periodic structures.

Optical characterization: We measure linear spectra of the nanostructures under normal incidence, in an Olympus IX-73 research microscope. Broadband illumination of the sample is performed with a 100 W halogen lamp (Olympus) which gives intensity in the visible and near-infrared spectral range. The polarization state is controlled with a Glan-Taylor polarizer, giving linearly polarized light. We measure the reflection spectra with a 50× objective of numerical aperture 0.5. The collected light is fiber-coupled to a spectrometer with a Peltier-cooled charge-coupled-device from Ocean Optics (QE65000 and NIRquest512 for visible and near-infrared measurements, respectively).

Surface enhanced Raman spectroscopy: SERS spectra are recorded with a Renishaw inVia micro-Raman spectrometer equipped with 150× LEICA HCX PL APO objective (numerical aperture 0.95), laser excitations at 830 nm, 785 nm, 633 nm, 532 nm, and a thermoelectrically cooled charge-coupled device (CCD) as a detector. Consequently, the laser spot diameter was around 680 nm, 800 nm, 1 μm, 1.07 μm for excitation wavelengths of 532 nm, 633 nm, 785 nm and 830 nm, respectively. The instrument is calibrated with respect to the first order silicon peak at 520 cm⁻¹, and all the spectra are recorded in backscattering

geometry at room temperature. The spectra are baseline corrected with a 3rd order polynomial by using Wire 3.0 software. The probe molecules (p-MA and Rhodamine) employed in this study are purchased from Sigma-Aldrich.

Analyte preparation: A stock solution of p-MA at 1 mM concentration is prepared by dissolving an appropriate amount of the solid analyte (Sigma-Aldrich) into 15 ml of ethanol. Afterward, 1 μ M to 1 fM solutions are prepared by a further dilution. For SERS measurements, molecules are deposited on to the substrate by chemisorption process. The samples are dipped for 20 min., then washed in ethanol to remove excess molecules that are not covalently bound to the metallic surface, and finally purged with nitrogen gas. In the case of R6G, the stock solution is prepared by diluting the molecules into deionized water.

Supporting Information

Supporting Information is available from the Wiley Online Library or from the author.

Acknowledgements

We acknowledge financial support from the Danish Council for Independent Research (the FTP project PlasTPV, contract no. 1335-00104). A. T. acknowledges support by Compagnia di San Paolo under grant agreement ID ROL 10262.

Received: ((will be filled in by the editorial staff))

Revised: ((will be filled in by the editorial staff))

Published online: ((will be filled in by the editorial staff))

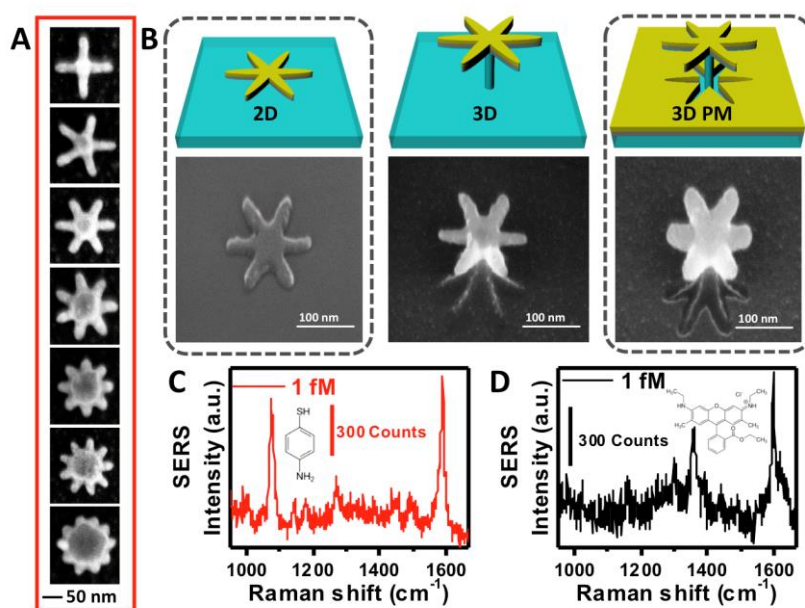
References

- [1] M. Moskovits, Nature 2011, 469, 307; R. Zhang, Y. Zhang, Z. C. Dong, S. Jiang, C. Zhang, L. G. Chen, L. Zhang, Y. Liao, J. Aizpurua, Y. Luo, J. L. Yang, J. G. Hou, Nature 2013, 498, 82; D. Punj, M. Mivelle, S. B. Moparthy, T. S. van Zanten, H. Rigneault, N. F. van Hulst, M. F. Garcia-Parajo, J. Wenger, Nat Nano 2013, 8, 512; A. Ahmed, R. Gordon, Nano Letters 2011, 11, 1800.
- [2] P. G. Etchegoin, E. C. Le Ru, Physical Chemistry Chemical Physics 2008, 10, 6079.
- [3] M. Chirumamilla, A. Toma, A. Gopalakrishnan, G. Das, R. P. Zaccaria, R. Krahne, E. Rondanina, M. Leoncini, C. Liberale, F. De Angelis and E. Di Fabrizio, Advanced Materials 2014, 26, 2353.
- [4] A. Gopalakrishnan, M. Chirumamilla, F. De Angelis, A. Toma, R. P. Zaccaria, R. Krahne, ACS Nano 2014, 8, 7986.

- [5] S. Harmsen, R. Huang, M. A. Wall, H. Karabeber, J. M. Samii, M. Spaliviero, J. R. White, S. Monette, R. O'Connor, K. L. Pitter, S. A. Sastra, M. Saborowski, E. C. Holland, S. Singer, K. P. Olive, S. W. Lowe, R. G. Blasberg, M. F. Kircher, *Science Translational Medicine* 2015, 7, 271ra7; A. Gopalakrishnan, M. Malerba, S. Tuccio, S. Panaro, E. Miele, M. Chirumamilla, S. Santoriello, C. Dorigoni, A. Giugni, R. Proietti Zaccaria, C. Liberale, F. De Angelis, L. Razzari, R. Krahne, A. Toma, G. Das, E. Di Fabrizio, *Annalen der Physik* 2012, 524, 620.
- [6] H. Xu, J. Aizpurua, M. Käll, P. Apell, *Physical Review E* 2000, 62, 4318; J. M. McLellan, Z.-Y. Li, A. R. Siekkinen, Y. Xia, *Nano Letters* 2007, 7, 1013; E. M. Perassi, E. A. Coronado, *The Journal of Physical Chemistry C* 2013, 117, 7744.
- [7] F. S. Ou, M. Hu, I. Naumov, A. Kim, W. Wu, A. M. Bratkovsky, X. Li, R. S. Williams, Z. Li, *Nano Letters* 2011, 11, 2538.
- [8] E. C. Le Ru, P. G. Etchegoin, M. Meyer, *The Journal of Chemical Physics* 2006, 125, 204701.
- [9] R. Schreiber, J. Do, E.-M. Roller, T. Zhang, V. J. Schuller, P. C. Nickels, J. Feldmann, T. Liedl, *Nat Nano* 2014, 9, 74; A. Hakonen, M. Svedendahl, R. Ogier, Z.-J. Yang, K. Lodewijks, R. Verre, T. Shegai, P. O. Andersson, M. Kall, *Nanoscale* 2015, 7, 9405; A. Toma, G. Das, M. Chirumamilla, A. Saeed, R. Proietti Zaccaria, L. Razzari, M. Leoncini, C. Liberale, F. De Angelis, E. Di Fabrizio, *Microelectronic Engineering* 2012, 98, 424.
- [10] M. Chirumamilla, G. Das, A. Toma, A. Gopalakrishnan, R. P. Zaccaria, C. Liberale, F. De Angelis, E. Di Fabrizio, *Microelectronic Engineering* 2012, 97, 189.
- [11] M. Hu, F. S. Ou, W. Wu, I. Naumov, X. Li, A. M. Bratkovsky, R. S. Williams, Z. Li, *Journal of the American Chemical Society* 2010, 132, 12820; M. S. Schmidt, J. Hübner, A. Boisen, *Advanced Materials* 2012, 24, OP11; X. Xu, K. Kim, H. Li, D. L. Fan, *Advanced Materials* 2012, 24, 5457.
- [12] D. Radziuk, H. Moehwald, *Physical Chemistry Chemical Physics* 2015, 17, 21072.
- [13] K. Jung, J. Hahn, S. In, Y. Bae, H. Lee, P. V. Pikhitsa, K. Ahn, K. Ha, J.-K. Lee, N. Park, M. Choi, *Advanced Materials* 2014, 26, 5924; C. Forestiere, A. J. Pasquale, A. Capretti, G. Miano, A. Tamburrino, S. Y. Lee, B. M. Reinhard, L. Dal Negro, *Nano Letters* 2012, 12, 2037; B. Yan, A. Thubagere, W. R. Premasiri, L. D. Ziegler, L. Dal Negro, B. r. M. Reinhard, *ACS Nano* 2009, 3, 1190; S. L. Kleinman, R. R. Frontiera, A.-I. Henry, J. A. Dieringer, R. P. Van Duyne, *Physical Chemistry Chemical Physics* 2013, 15, 21; L. Fabris, *Chemical Communications* 2012, 48, 9346; M. Chirumamilla, A. Gopalakrishnan, A. Toma, R. P. Zaccaria, R. Krahne, *Nanotechnology* 2014, 25, 235303; H. Yuan, C. M. Wilson, J. Xia, S. L. Doyle, S. Li, A. M. Fales, Y. Liu, E. Ozaki, K. Mulfaul, G. Hanna, G. M. Palmer, L. V. Wang, G. A. Grant, T. Vo-Dinh, *Nanoscale* 2014, 6, 4078.
- [14] A. Shiohara, Y. Wang, L. M. Liz-Marzán, *Journal of Photochemistry and Photobiology C: Photochemistry Reviews* 2014, 21, 2.
- [15] M. Valamanesh, Y. Borensztein, C. Langlois, E. Lacaze, *The Journal of Physical Chemistry C* 2011, 115, 2914.
- [16] M. W. Knight, Y. Wu, J. B. Lassiter, P. Nordlander, N. J. Halas, *Nano Letters* 2009, 9, 2188.
- [17] C. Huck, A. Toma, F. Neubrech, M. Chirumamilla, J. Vogt, F. De Angelis, A. Pucci, *ACS Photonics* 2015, 2, 497.
- [18] A. E. Cetin, D. Etezadi, H. Altug, *Advanced Optical Materials* 2014, 2, 866; H. Chen, A. M. Bhuiya, R. Liu, D. M. Wasserman, K. C. Toussaint, *The Journal of Physical Chemistry C* 2014, 118, 20553.
- [19] L. Rivas, S. Sanchez-Cortes, J. V. García-Ramos, G. Morcillo, *Langmuir* 2000, 16, 9722; W. Zhang, M. Rahmani, W. Niu, S. Ravaine, M. Hong, X. Lu, *Scientific Reports* 2015, 5, 8382.

- [20] W. Rechberger, A. Hohenau, A. Leitner, J. R. Krenn, B. Lamprecht, F. R. Aussenegg, *Optics Communications* 2003, 220, 137.
- [21] A. Curry, G. Nusz, A. Chilkoti, A. Wax, *Optics Express* 2005, 13, 2668.
- [22] Y. Shen, J. Zhou, T. Liu, Y. Tao, R. Jiang, M. Liu, G. Xiao, J. Zhu, Z.-K. Zhou, X. Wang, C. Jin, J. Wang, *Nat Commun* 2013, 4; K. Kumar, H. Duan, R. S. Hegde, S. C. W. Koh, J. N. Wei, J. K. W. Yang, *Nat Nano* 2012, 7, 557.
- [23] A. Dmitriev, C. Hägglund, S. Chen, H. Fredriksson, T. Pakizeh, M. Käll, D. S. Sutherland, *Nano Letters* 2008, 8, 3893; K. C. Vernon, A. M. Funston, C. Novo, D. E. Gómez, P. Mulvaney, T. J. Davis, *Nano Letters* 2010, 10, 2080.
- [24] A. Tittl, P. Mai, R. Taubert, D. Dregely, N. Liu, H. Giessen, *Nano Letters* 2011, 11, 4366.
- [25] T. W. Ebbesen, H. J. Lezec, H. F. Ghaemi, T. Thio, P. A. Wolff, *Nature* 1998, 391, 667; J. Li, J. Ye, C. Chen, L. Hermans, N. Verellen, J. Ryken, H. Jans, W. Van Roy, V. V. Moshchalkov, L. Lagae, P. Van Dorpe, *Advanced Optical Materials* 2015, 3, 176.
- [26] K. Katrin, K. Harald, I. Irving, R. D. Ramachandra, S. F. Michael, *Journal of Physics: Condensed Matter* 2002, 14, R597.
- [27] S. M. Mahurin, J. John, M. J. Sepaniak, S. Dai, *Appl. Spectrosc.* 2011, 65, 417.

ToC figure



Supporting Information

DOI: 10.1002/ ((please add manuscript number))

Article type: Full Paper

Hot-spot Engineering in 3D Multi-branched Nanostructures: Ultrasensitive Substrates for Surface Enhanced Raman Spectroscopy

Manohar Chirumamilla, Anisha Chirumamilla, Alexander S. Roberts, Remo Proietti Zaccaria, Francesco De Angelis, Peter Kjær Kristensen, Roman Krahne, Sergey I. Bozhevolnyi, Kjeld Pedersen and Andrea Toma**

Dr. M. Chirumamilla, Dr. P. Kjær Kristensen, Prof. K. Pedersen

Department of Physics and Nanotechnology, University of Aalborg, Skjernvej 4A, Aalborg, 9220, Denmark

E-mail: mch@nano.aau.dk

Dr. A. Chirumamilla, Prof. R. Proietti Zaccaria, Dr. F. De Angelis, Dr. R. Krahne, Dr. A. Toma,

Istituto Italiano di Tecnologia, Via Morego 30, Genova, 16163, Italy

E-mail: andrea.toma@iit.it

Mr. A. S. Roberts, Prof. S. I. Bozhevolnyi

Institute of Technology & Innovation, University of Southern Denmark, Niels Bohrs Allé 1, Odense, 5230, Denmark

Keywords: Hotspot engineering, 3D multibranch nanostar structures, plasmonics, electron beam lithography, Single Molecule Surface enhanced Raman scattering

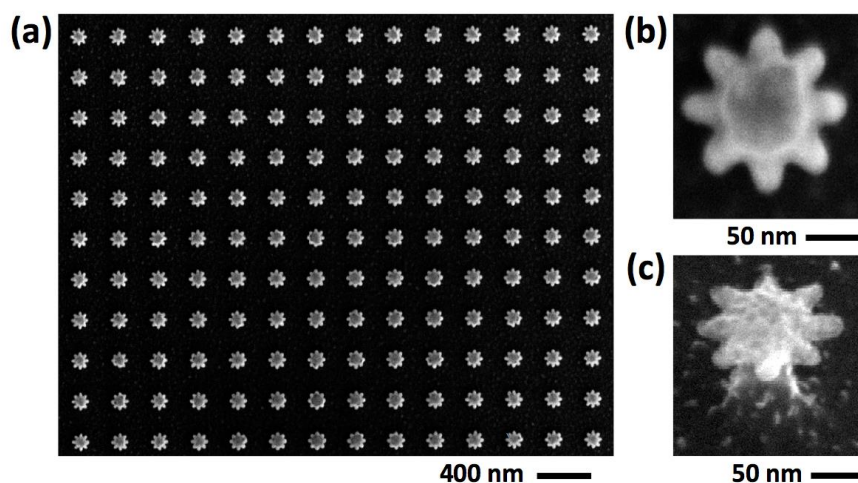


Figure SII. SEM images of 3D MBNS, S8 layout: In order to perform far-field spectroscopy, we fabricated $25\ \mu\text{m} \times 25\ \mu\text{m}$ size matrices of planar, 3D MBNS and 3D MBNS PM nanostars, each of them at a mutual distance of 340 nm in both directions. The homogeneity and uniformity of the fabricated nanostructures is highlighted by the SEM micrograph reported in (a). b, c) represent the magnified view of a single S8 nanostructure, top and tilted view, respectively.

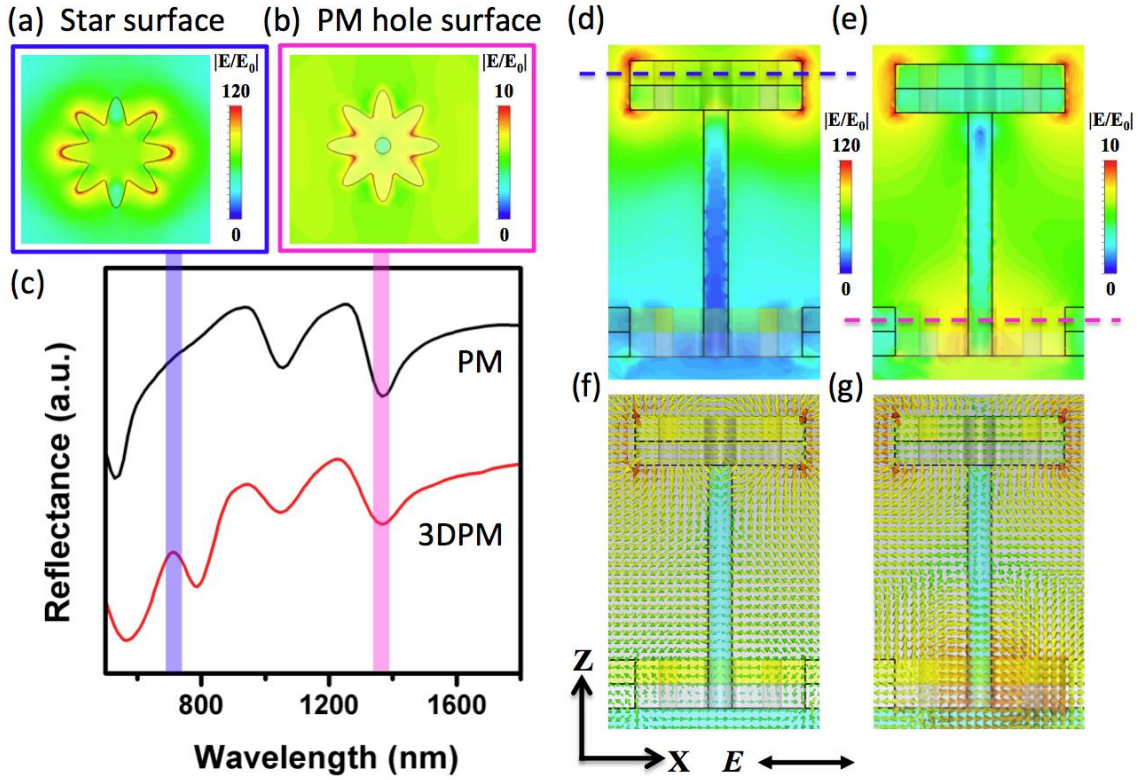


Figure SI2. Comparison between 3D MBNS PM and PM hole topologies: the optical response of the S8 architecture with PM hole and 3D MBNS PM topologies has been numerically evaluated. For 3D MBNS with PM layer, the electric field (Figure SI2a – top view and Figure SI2d – side view) and the surface current distributions (Figure SI2f) at 650 nm show a dipolar behavior with strong electric field localization at the nanostructure ends. As clearly highlighted by the far-field spectral behavior (Figure SI2c black and red traces), the peak at 650 nm appears only in the MBNS layout. Therefore, the present mode can be associated to the localized surface plasmon resonance of the 3D nanostar. On the contrary, for the reflection minimum at 1350 nm, the electric field (Figure SI2b – top view and Figure SI2e – side view) and the surface current distributions (Figure SI2g) are strongly localized at the sharp inward edges of the PM holes. This configuration can be ascribed to the localized surface plasmon resonance supported by the PM cavity. The blue and purple dashed lines in Figure SI2d and SI2e indicate the regions where the top view cut-outs (Figure SI2a and SI2b, respectively) have been evaluated.

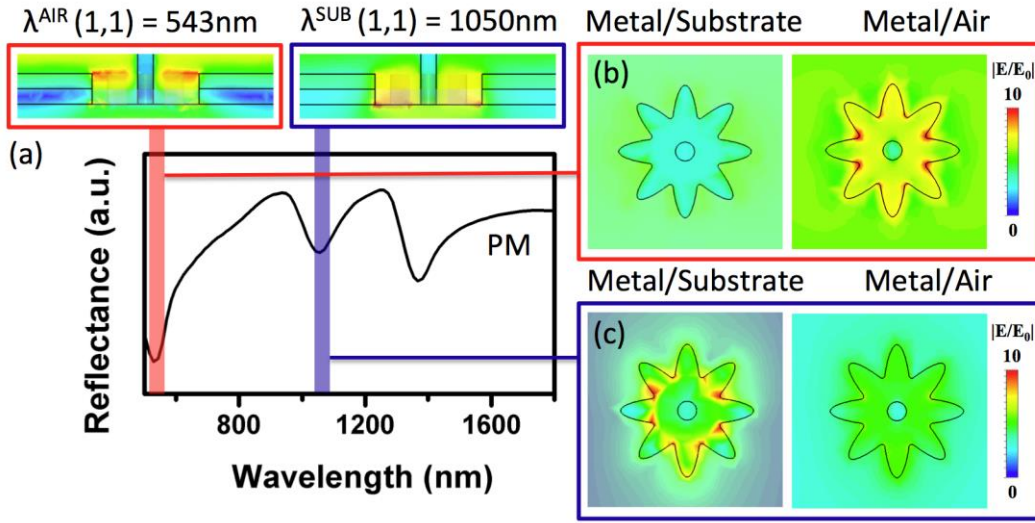


Figure SI3. Resonant Modes supported by PM structures: the star-shaped hole in the PM layer behaves like a plasmonic cavity and allows the excitation of LSPR as well as surface plasmon polaritons (SPPs) propagating at the metal/air and metal/substrate interfaces. The origin of the observed modes can be explained by calculating the near- and far-field responses of a PM layer alone (without 3D MBNS structures). By taking into account the momentum matching condition for perforated metallic holes (*i.e.* the Bragg's equation) we can obtain for a two-dimensional lattice:

$$k_0 \sin \theta \pm iG_x \pm jG_y = k_{modes}$$

and accordingly the SPP mode can be described by:

$$\lambda_{SPP} \cong \frac{p}{\sqrt{i^2 + j^2}} \sqrt{\frac{\epsilon_m \epsilon_d}{\epsilon_m + \epsilon_d}}$$

Where G_x and G_y are the reciprocal lattice vectors, i and j the grating orders, θ and k_0 the angle and the wavenumber of the incident light, p is the periodicity of the hole array and ϵ_m , ϵ_d are the dielectric functions of the metal and the surrounding medium. For a periodicity of 340 nm, SPPs excited at the metal/substrate interface show a reflection minimum at 1050 nm (Blue boxes in Figure SI3), which can be ascribed to the mode $\lambda_{(1,1)}^{SUB}$. On the contrary, SPPs propagating at the metal/air interface $\lambda_{(1,0)}^{AIR}$ and $\lambda_{(1,1)}^{AIR}$ can be seen at 750 nm and 543 nm (Red boxes in Figure SI3), respectively. The physical origin of $\lambda_{(1,1)}^{AIR}$ and $\lambda_{(1,1)}^{SUB}$ modes is depicted by the near-field distributions presented in Figure. For instance at the $\lambda_{(1,1)}^{AIR}$ resonance, the electric field distribution at the metal/substrate and metal/air interfaces (Figure SI3b) confirm that there is strong field localization to the metal/air interface (Figure SI3a, b). Similarly, for the $\lambda_{(1,1)}^{SUB}$ resonance, the field is localized to the metal/substrate interface (Figure SI3a, c).

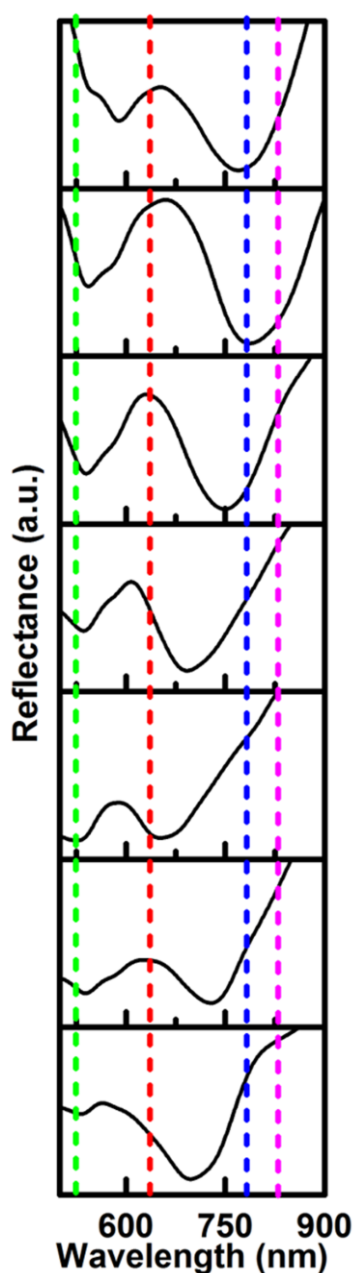


Figure SI4. Reflection spectra of 3D MBNS PM structures with different number of branches: the optical response of 3D nanostars with 4 to 10 branches (bottom to top, respectively) is reported in Figure SI4. Dashed lines (green, red, blue and magenta) indicate the excitation laser lines (532, 633, 785 and 830 nm) available for SERS measurements. In 3D nanostructures, the plasmon resonance strongly depends on the Si nanopiedestal. Therefore, the anisotropic etching of the Si pillar, due to the different nanostructure geometries, leads to an irregular trend, contrary to what is observed for 2D nanostructures.

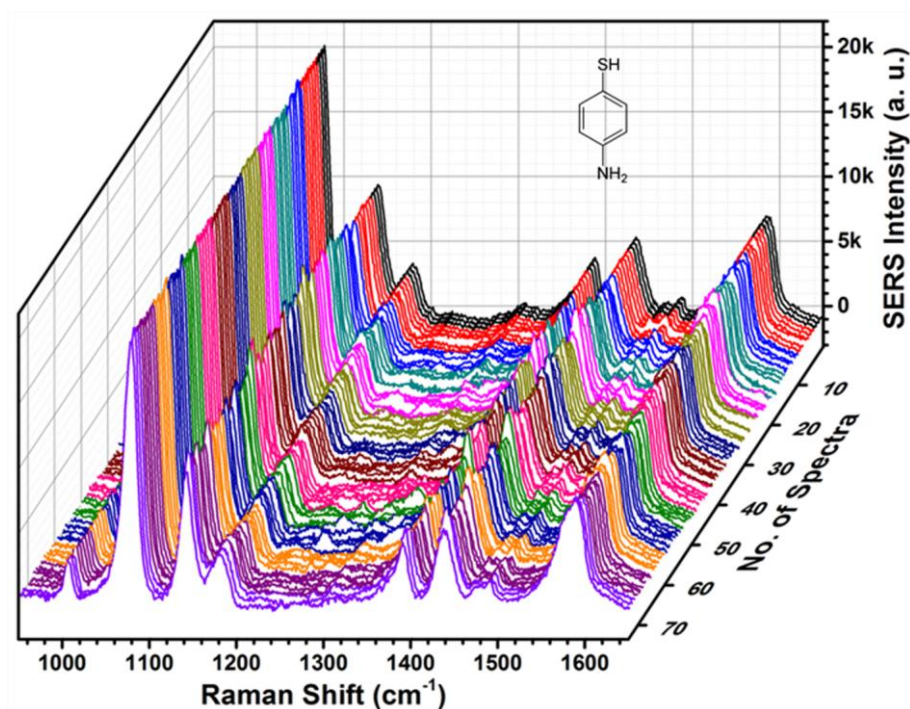


Figure SI5. SERS spectra of p-MA molecules: 3D waterfall spectra of p-MA (1 μ M concentration) on 3D MBNS PM with S8 geometry have been recorded from around 70 different spatial positions of the same sample. The incident laser, accumulation time and power are set to 785 nm, 1 mW and 3 s, respectively.

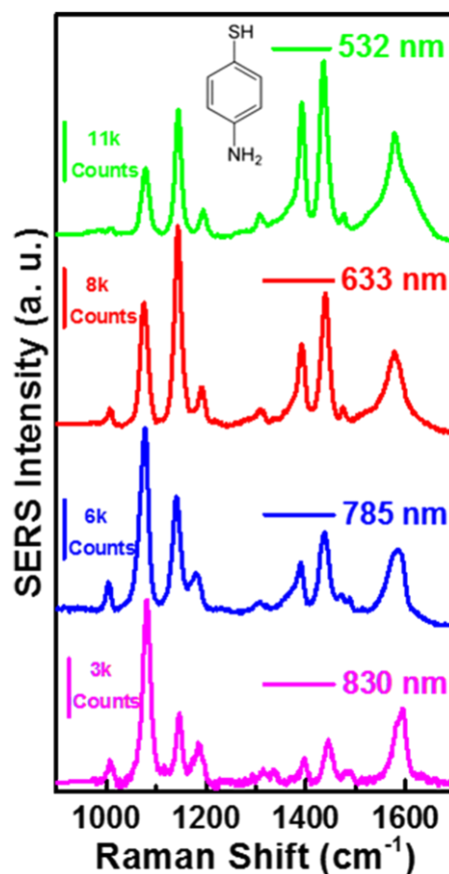


Figure SI6. SERS spectra acquired with different excitation sources: typical SERS spectra of p-MA (1 μ M concentration) taken on 3D MBNS PM structures with S8 geometry for 532, 633, 785 and 830 nm excitation laser lines, represented by green, red, blue and magenta traces, respectively. The accumulation time is set to 3 s.

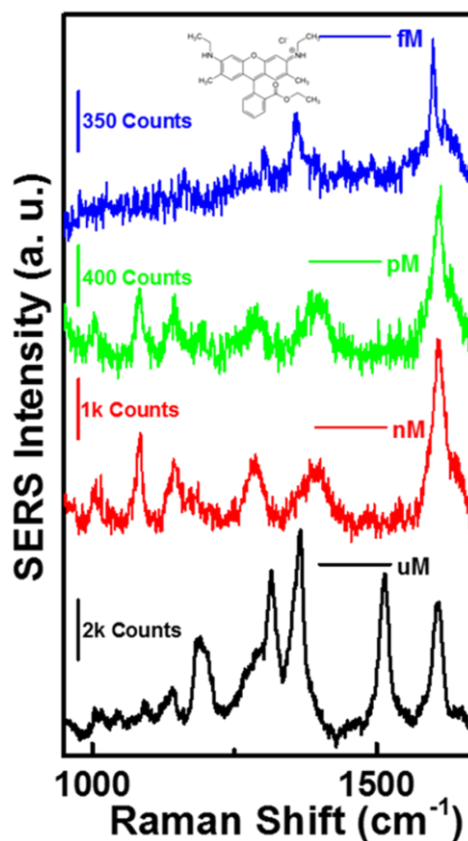


Figure SI7. SERS spectra of R6G molecules: typical SERS spectra of R6G recorded on 3D MBNS PM structures with S8 geometry at molecular concentrations of 1 μM , 1 nM, 1 pM and 1 fM, depicted by black, red, green and blue traces, respectively. The laser excitation, power and accumulation time are set to 830 nm, 10 mW and 3 s, respectively.

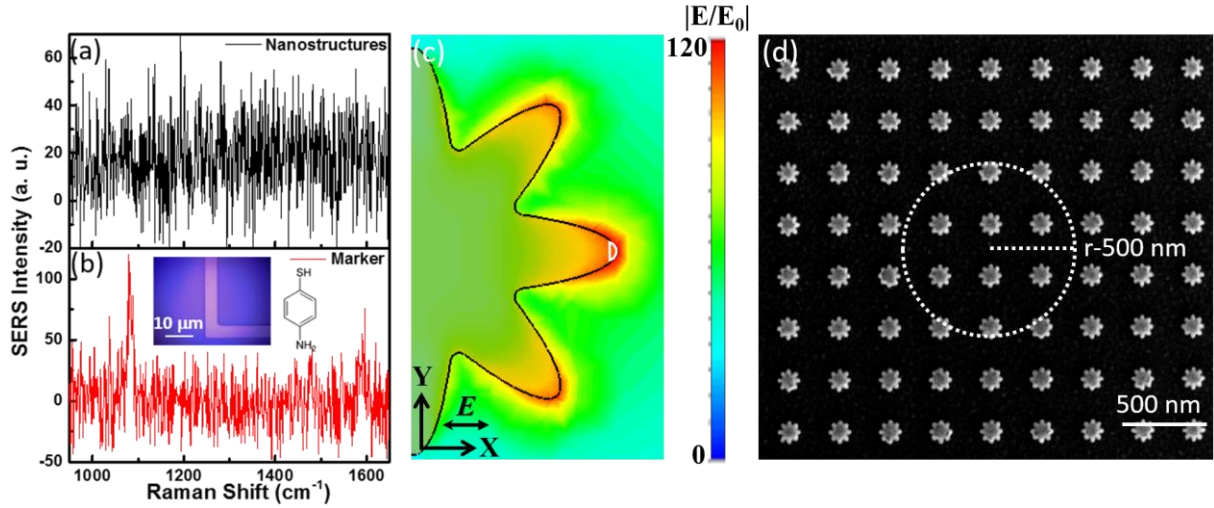


Figure SI8. SERS enhancement factor calculation: a) Background Raman spectrum was taken on 3D MBNS PM with S8 architectures before chemisorption of p-MA molecules. b) Reference Raman spectrum of p-MA (1 μ M concentration) recorded on an L-shaped marker. The laser excitation, power and accumulation time are set to 785 nm, 1 mW and 30 s, respectively.

SERS enhancement factor calculation

The SERS enhancement factor (EF), has been calculated using the following expression,

$$EF = \frac{I_{SERS}}{I_{Raman}} \cdot \frac{A_{Raman}}{A_{SERS}} \cdot \frac{P_{Raman}}{P_{SERS}} \cdot \frac{t_{Raman}}{t_{SERS}} \quad (\text{eq. S1})$$

where I , A , P and t are the peak height, the area of the structure, the laser power and the accumulation time. The subscripts *Raman* and *SERS* stand for measurements performed on planar metal films and MBNS nanostructures, respectively. In each case, incident power and accumulation time were kept constant.

According to Le Ru et al.^[1] the SERS signal is essentially provided by the molecules adsorbed at positions with strongly enhanced EM fields. For such a reason, in order to evaluate A_{SERS} we have considered the local surface area^[2] of every hot spots (see Figure SI8c, half-circle surrounded by white line $\sim 14 \text{ nm}^2$ for each protrusion). From the Figure 2e and SI8c, it is clear that only 6 tips contribute to the SERS signal (for an 8-branched MBNS under linear polarization along x-axis). Moreover, the average field enhancement along the branches placed at an angle of 45° is decreased by a factor of 2. In view of that, the effective area for a single nanostar is $\sim 56 \text{ nm}^2$. By considering 7 nanostars excited under the laser spot (Figure SI8d - incident laser beam with 500 nm radius), we can obtain $A_{SERS} = 7 \times 56 \text{ nm}^2 = 3.92 \times 10^{-16} \text{ m}^2$,

For the reference spectrum A_{Raman} corresponds to the illumination spot size:

$$A_{Raman} = 3.14 \times (500 \text{ nm})^2 = 7.85 \times 10^{-13} \text{ m}^2$$

The experimental values of I , P and t for SERS and Raman are taken from Figure 4a and Figure SI8, respectively:

$$I_{SERS} = 260100 \text{ (counts)} \text{ and } I_{Raman} = 100 \text{ (counts)}. \text{ Therefore, } EF = 5.2 \times 10^6$$

It is worth to be noticed that the planar AgAu films are acting as SERS substrates with an enhancement factor EF' (evaluated by considering a non-enhancing Raman substrate) which can be calculated as:

$$G' = \frac{I_{Raman}}{I_{Bulk}} \cdot \frac{N_{Bulk}}{N_{Raman}} \cdot \frac{P_{Bulk}}{P_{Raman}} \cdot \frac{t_{Bulk}}{t_{Raman}} \quad (\text{eq. S2})$$

where I , N , P and t represent the peak height, the number of molecules, the laser power and the accumulation time. The subscripts *Bulk* and *Raman* indicate measurements performed on a non-enhancing Raman substrate and a planar metal film, respectively. $N_{Bulk} = 3.3 \times 10^{10}$ has been estimated by considering the focusing volume of the laser spot and the density of p-MA (1.06 g/cm^3).^[3] N_{Raman} has been calculated by considering the same active area employed in eq. S1 (A_{Raman}) and a packing density of $0.2 \text{ nm}^2/\text{molecule}$ for the p-MA.^[3] The estimated absolute enhancement factor is $EF' = EF \times G' = 1.6 \times 10^{11}$.

References

- [1] E. C. Le Ru, P. G. Etchegoin, M. Meyer, *The Journal of Chemical Physics* 2006, 125, 204701.
- [2] C. Hrelescu, T. K. Sau, A. L. Rogach, F. Jackel, J. Feldmann, *Applied Physics Letters* 2009, 94, 153113; M. Chirumamilla, A. Toma, A. Gopalakrishnan, G. Das, R. P. Zaccaria, R. Krahne, E. Rondanina, M. Leoncini, C. Liberale, F. De Angelis and E. Di Fabrizio, *Advanced Materials* 2014, 26, 2353.
- [3] N. A. Hatab, C.-H. Hsueh, A. L. Gaddis, S. T. Retterer, J.-H. Li, G. Eres, Z. Zhang, B. Gu, *Nano Letters* 2010, 10, 4952; J. B. Jackson, N. J. Halas, *Proceedings of the National Academy of Sciences* 2004, 101, 17930.